HAL open science

Retrieval of Mars surface physical properties from OMEGA hyperspectral images using Regularized Sliced Inverse Regression.

Caroline Bernard-Michel, Sylvain Douté, Mathieu Fauvel, Laurent Gardes, Stéphane Girard

To cite this version:

Caroline Bernard-Michel, Sylvain Douté, Mathieu Fauvel, Laurent Gardes, Stéphane Girard. Retrieval of Mars surface physical properties from OMEGA hyperspectral images using Regularized Sliced Inverse Regression.. [Research Report] 2008, pp.43. inria-00276116v2

HAL Id: inria-00276116

https://inria.hal.science/inria-00276116v2

Submitted on 6 Nov 2008

HAL is a multi-disciplinary open access archive for the deposit and dissemination of scientific research documents, whether they are published or not. The documents may come from teaching and research institutions in France or abroad, or from public or private research centers.

L'archive ouverte pluridisciplinaire **HAL**, est destinée au dépôt et à la diffusion de documents scientifiques de niveau recherche, publiés ou non, émanant des établissements d'enseignement et de recherche français ou étrangers, des laboratoires publics ou privés.

JOURNAL OF GEOPHYSICAL RESEARCH, VOL. ???, XXXX, DOI:10.1029/,

Retrieval of Mars surface physical properties from OMEGA hyperspectral images using Regularized Sliced Inverse Regression

C. Bernard-Michel[1], S. Douté[2], M. Fauvel[1], L. Gardes[1], and S. Girard[1]

C. Bernard-Michel, M. Fauvel, L. Gardes and S. Girard, MISTIS, INRIA Rhône-Alpes, Montbonnot, Inovallée, 655 avenue de l'Europe, 38 334 Saint Ismier Cedex, France.

S. Douté, Laboratoire de Planétologie de Grenoble, Bât. D de Physique, B.P. 53, 38041 Grenoble Cedex 9, France. (sylvain.doute@obs.ujf-grenoble.fr)

[1]MISTIS, INRIA Rhône-Alpes,

Montbonnot, France.

[2]Laboratoire de Planétologie de Grenoble,

Saint Martin-d'Hères, France.

Abstract. In this paper, a statistical method is proposed to evaluate the physical properties of surface materials on Mars from hyperspectral images collected by the OMEGA instrument aboard the Mars express spacecraft. The approach is based on the estimation of the functional relationship F between some observed spectra and some physical parameters. To this end, a database of synthetic spectra is generated by a physical radiative transfer model and used to estimate F. The high dimension of spectra is reduced by Gaussian regularized sliced inverse regression (GRSIR) to overcome the curse of dimensionality and consequently the sensitivity of the inversion to noise (ill-conditioned problems). Compared with other approaches, GRSIR has the advantage of being very fast, interpretable and accurate.

1. Introduction

Visible and near infrared imaging spectroscopy is a key remote sensing technique used to study and monitor planets. It allows the detection, mapping and characterization of minerals, as well as volatile species, that often constitute the first step toward the resolution of key climatic and geological issues [*Murchie et al.*, 2007; *Bibring et al.*, 2004a; *Brown et al.*, 2004; *Carlson et al.*, 1992]. These tasks are carried out through spectral analysis of solar light reflected by the material forming the top few millimeters or centimeters of the ground. Physical properties of the surface, such as chemical composition, granularity, texture, and physical state are some of the most important parameters that characterize the morphology of spectra. Modeling the direct link between these parameters and observable spectra is called the *forward problem* in classical physics. It can be evaluated numerically by radiative transfer models, simulating the propagation of solar light through the atmosphere and reflected back to the sensor [*Douté et al.*, 2007b; *Hapke*, 2002; *Shkuratov et al.*, 1999; *Douté and Schmitt*, 1998; *Hapke*, 1993]. Such a model allows the simulation of spectra from given values of the model parameters. Conversely, deducing the physical model parameters from the observed spectra is called an *inverse problem*. Since it generally cannot be solved analytically, the use of optimization or statistical methods is necessary. Solving inverse problems requires an adequate understanding of the fundamental physics, so that a relation $X = G(Y)$ may be specified between the spectra X and the parameters Y. Given G, different methods can be used to deduce the parameters Y from the observation X. Current solutions to the inverse problem can be

divided into three main categories (for further details and comparisons, see [*Kimes et al.*, 2000; *Pragnère et al.*, 1999]):

1. *Optimization algorithms*: These methods minimize an objective function that expresses the quality of the estimations, and include numerical optimization techniques such as Powell's method, Simplex method and the quasi-Newton method. Estimation can be unstable since inverse problems are often ill-posed (solutions are not unique, and a small change in the data can lead to large differences in the estimations). A probabilistic formalism can be used to regularize inverse problems by introducing a prior distribution on model parameters [*Aster et al.*, 2005; *Tarantola*, 2005]. These approaches are computationally expensive since they independently invert new spectra. Therefore, they cannot be used to invert an image with several hundred thousand pixels. Moreover, they can sometimes fall into local minima if the objective function is not convex.

2. *Look-up table (LUT) / k-nearest neighbors approach (k-NN)*: This methodology is currently used by physicists to study planetary bodies [*Carlson et al.*, 2005; *Philpot et al.*, 2004; *Weiss et al.*, 2000; *Douté et al.*, 2001]. The previous heavy runtime computation is replaced by a simpler look-up operation. A large database (LUT) is generated by radiative transfer for many parameter values. To invert an hyperspectral image, the pixel's spectrum is then compared with the LUT spectra in order to find the best match (the nearest neighbor), according to an objective function minimization. Parameters are then deduced from this best match. The speed gain is significant in comparison to traditional optimization methods, since retrieving a value from memory is often faster than undergoing an expensive computation. The main disadvantages of this approach are the multiplicity of solutions and their instability [*Bernard-Michel et al.*, 2007].

3. *Training approaches*: They have been recently considered in the study of terrestrial vegetation. A functional relationship

$$Y = F(X) \tag{1}$$

between spectra and parameters is assumed. This relationship corresponds to the inverse of the physical model G in the forward problem. The idea is to use a LUT to estimate the underlying mathematical relationship F. This relationship then allow us to estimate the parameters of new spectra. The advantage of such a training approach is that, once the relationship has been established, it can be used for very large sets and for all new images with the same physical model. Among training approaches, neural networks [*Hastie et al.*, 2003, chapter 11] or support vector machines (SVM) [*Hastie et al.*, 2003, chapter 12] seem promising but the underlying learning process remains time consuming [*Combal et al.*, 2002; *Durbha et al.*, 2007; *Pragnère et al.*, 1999].

Hyperspectral images on planets must be inverted with the following constraints: 1. Working with large data-sets and various models require fast methodologies, 2. When dealing with very high-dimensional data, one is faced with the 'curse of dimensionality' and the associated sparsity issues and, 3. Observed spectra always contain some noise.

In this paper, a new training approach is proposed: The Gaussian Regularized Sliced Inverse Regression (GRSIR)[*Bernard-Michel et al.*, to appear, 2008]. It is based on a dimension reduction technique first proposed by [*Li*, 1991] and similar to Partial Least Squares regression (PLS), [*Hastie et al.*, 2003, chapter 3]. It has the advantage of being fast, stable, statistically and physically interpretable, and can also help to select an appropriate look-up table for inversion. For the sake of validation, this approach is compared with k-NN, PLS and SVM.

In Section 2, real and simulated data-sets are presented, then the principle of GRSIR is recalled in Section 3. The choice of an appropriate LUT is discussed in Section 4. Experimental results are presented on simulated data-sets in Section 5 and on real Mars images in Section 6. Conclusions are drawn in Section 7.

2. Data

The data-sets used in the next sections can be divided in three categories: The hyperspectral images observed on Mars, a LUT simulated by radiative transfer algorithms according to some physical modeling of these images, and test data in order to quantify the according of the estimation. All data-sets consist of some spectra $X \in \mathbb{R}^d$ with associated parameters $Y \in \mathbb{R}^p$, d being the number of wavelengths and p the number of parameters.

2.1. Hyperspectral images from Mars

The data-sets were collected by the imaging spectrometer OMEGA (Observatoire pour la Minéralogie, l'Eau, la Glace et l'Activité) [*Bibring et al.*, 2004a]. OMEGA is one of the seven scientific instruments aboard the European spacecraft Mars Express mission, sent to orbit Mars in 2003. It was developed by IAS and LESIA (Observatoire de Paris) with the support of CNES, and with the participation of IFSI (Italy) and IKI (Russia). This visible and infrared instrument can scan most of Mars from orbit in order to observe gas and dust in the atmosphere and look for signs of specific materials such as silicates, carbonates and ice at the surface. It records the visible and infrared light reflected from the planet in the 0.5-5.2 micron wavelength range and with a ground resolution varying from 350 m to 10 km. Three OMEGA hyperspectral images acquired during orbits 41, 61 and 103

will be used. They cover the high southern latitudes of Mars. The spatial resolution is approximately 2km per pixel and 184 wavelengths have been considered in the range 0.95-4.15 (*i.e.* $d = 184$). For each spectrum of the image, the atmospheric gaseous contribution has been removed [*Douté et al.*, 2007b]. After a first analysis, these OMEGA observations revealed that the south polar region of Mars exhibits mainly water ice, carbon dioxide ice and dust at the surface [*Bibring et al.*, 2004b]. A detailed qualitative mapping of the ice during the local summer shows that the permanent bright cap is dominated by superficial CO_2 ice. Nevertheless, its spectral signature is slightly contaminated by the contribution of dust and water ice. Among the possible coexistence modes of the latter components, a granular mixture of H_2O, CO_2 ice and dust is the most appropriate to reproduce the morphology of the spectra [*Douté et al.*, 2007a]. This conclusion is based on numerical experiments that aimed at reproducing the spectra by different surface reflectance models. The permanent polar cap has been mapped by a classification method based on wavelets [*Schmidt et al.*, 2007]. For each image, the CO_2 ice areas contain about 10000 to 20000 spectra. The selected model for the polar cap considers the intimate mixture of H_2O, CO_2 ice and dust as an optically thick parallel layer without substantial roughness. The transfer of solar photons through such a material is calculated by a modified version of the Hapke semi-empirical formulation [*Hapke*, 2002; *Douté and Schmitt*, 1998; *Hapke*, 1993].

2.2. Look-up table (LUT)

The model implies five spatially varying parameters (*i.e.* $p = 5$): the grain size of water and CO_2 ice, the proportion of water ice, CO_2 ice and dust. The proportions are normalized to sum to one. The other parameters involved in the physical model, such as the incidence and emergence angles or the grain size of dust have been fixed to a constant.

Since *a priori* knowledge on the parameters range is unavailable, the simulation of a large look-table (LUT) is necessary. Details of the sampling strategy are provided in Table 1. The notation used in this article is as follows: n is the number of simulated spectra ($n = 31500$), $x_i \in \mathbb{R}^{184}$ denotes a spectrum from the LUT and $y_i \in \mathbb{R}^5$ its associated parameters, where $i \in \{1, \ldots, n\}$.

2.3. Test data

For validation and comparison, the use of a test data-set (Tdata) is required. Since no ground truth is currently available for the physical properties of Mars polar regions, we can only rely on synthetic data. The same physical model is used to simulate the LUT and Tdata. The range of variation for the parameter is detailed in Table 1. To emulate real data, a zero mean multiGaussian noise of dimension 184 is added to all the spectra of the test data-set. The covariance matrix is determined experimentally from a small, spatially homogeneous, portion of the real image. Assuming that much of the variability comes from the noise, the latter is then evaluated using statistics based on a shift difference on the selected portion. As in the previous section, n_T is the number of simulated test spectra ($n_T = 3500$), x_i^T is a spectrum from Tdata and y_i^T its associated parameters, where $i \in \{1, \ldots, n_T\}$.

3. Proposed approach

Our goal is to estimate the functional relationship F between the spectra $X \in \mathbb{R}^d$ and each physical parameter $Y^j = F(X) \in \mathbb{R}$ with $j \in \{1, \ldots, p\}$. In this work, each parameter is studied individually, therefore $p = 1$ and j will be omitted for the sake of simplicity. The originality of the methodology is to split the difficult problem of learning

a d-variate function into two sub-problems that can be easily solved. First, a dimension reduction technique is applied (Section 3.1). Then, estimation is performed in the lower dimensional subspace (Section 3.2).

3.1. Dimension reduction step: Gaussian regularized sliced inverse regression

Dimension reduction methods rely on the assumption that the predictor X can be replaced, without loss of information, by its projection onto a subspace of smaller dimension L, called the effective dimension reduction space (EDR). The basis of the subspace is denoted $\beta_1, \ldots, \beta_L$ and the functional relationship $Y = F(X)$ can be rewritten as $Y = f(\beta_1^t X, \ldots, \beta_L^t X)$, where f is now a L-variate function. In most applications, L is smaller than 3 making the estimation of f tractable.

Principal Component Analysis (PCA) is a classical approach to reduce the dimension [*Hastie et al.*, 2003, chapter 14]. The basic concept of PCA is to define the orthogonal projection of the spectra onto a lower dimensional linear space such that the total variance of the projected spectra is maximized. It amounts to diagonalization of the spectra covariance matrix

$$\Sigma = \frac{1}{n}\sum_{i=1}^{n}(x_i - \bar{x})(x_i - \bar{x})^t \text{ where } \bar{x} = \frac{1}{n}\sum_{i=1}^{n} x_i, \tag{2}$$

or equivalently to calculation of the eigenvectors of Σ. However, in regression problems PCA is generally not satisfactory since only the explanatory variable X is considered while the dependent variable Y is not taken into account. Specific dimension reduction techniques have been developed for regression problems, such as PLS and Sliced Inverse Regression (SIR) [*Li*, 1991]. SIR consists of sorting the parameter values in increasing order and dividing them into H non-overlapping slices $S_h, h \in \{1, \ldots, H\}$. For each slice

S_h, a mean spectrum m_h is calculated as the mean value of the parameter values that are varying in the slice. The orthogonal projection of the mean spectra onto a lower dimensional linear space is defined so that the variance of the projected mean spectra is maximized under the constraint that the total projected variance is one. This is equivalent to diagonalization of $\Sigma^{-1}\Gamma$, where Γ is the mean spectra covariance matrix given in equation (3). The SIR principle is illustrated in Figure 1.

Since inverse problems are generally ill-posed [*Aster et al.*, 2005; *Tarantola*, 2005], Σ is ill-conditioned, making its inversion difficult. To solve this problem, it is proposed to compute a Gaussian Regularized version of Sliced Inverse Regression (GRSIR). Theoretical foundations can be found in [*Bernard-Michel et al.*, to appear, 2008]. The concept of this method is to include some prior information on the projections in order to dampen the effect of noise in the input data. The ill-posed problem is then replaced by a slightly perturbed well-posed problem that depends on a regularization parameter δ. Therefore, GRSIR computes the L eigenvectors corresponding to the L largest eigenvalues of $(\Sigma^2 + \delta I_p)^{-1}\Sigma\Gamma$ where I_p is the $d \times d$ identity matrix. In practice, GRSIR then requires the three following computational steps:

Step 1: Sort $y_i, i \in \{1, \ldots, n\}$ into increasing order and divide into H non-overlapping slices S_h, $h = 1, \ldots, H$. If the LUT has been simulated for random values of Y, then slices are chosen such that each slice contains the same number of observations. If the LUT has been simulated for a fixed number of distinct parameters, the slices are chosen to coincide with these discrete values.

Step 2: Compute the "between slices" covariance matrix of the means:

$$\Gamma = \sum_{h=1}^{H} \frac{n_h}{n}(m_h - \bar{x})(m_h - \bar{x})^t \text{ with } m_h = \frac{1}{n_h} \sum_{y_i \in S_h} x_i, \tag{3}$$

where n_h denotes the number of observations in the slice S_h.

Step 3: Estimate the GRSIR axes $\beta_1(\delta), \ldots, \beta_L(\delta)$ by computing the eigenvectors of $(\Sigma^2 + \delta I_p)^{-1}\Sigma\Gamma$. The first GRSIR axis, $\beta_1(\delta)$, is determined by the eigenvector corresponding to the largest eigenvalue, the second GRSIR axis, $\beta_2(\delta)$, is determined by the eigenvector corresponding to the second largest eigenvalue, and so on.

In Section 5.4, a criterion to choose the dimension L is given. Interestingly, the first axis can be viewed as a weighted function of the wavelengths, giving some knowledge about the wavelengths that carry information on the parameter (Section 5.5). The projections of the spectra on the axis $\beta_1(\delta)$ is termed "reduced spectra".

3.2. Estimation of the functional relationship

One the spectra have been reduced, the relationship f has to be estimated. In the proposed approach, a piecewise linear interpolation is performed on the set of data points $(m_h^{proj}, m_h^{param})$, $h = 1, \ldots, H$, where $m_h^{proj} = \langle x_i, \beta_1(\delta)\rangle$ denotes the average of the projection of the spectra x_i, $y_i \in S_h$ for slice S_h and $m_h^{param} = \frac{1}{n_h}\sum_{y_i \in S_h} y_i$ denotes the average parameter value for slice S_h.

For each new spectrum x with a projection $t = \langle \beta_1(\delta), x\rangle$, the estimated parameter value $\hat{y}$ is then given by:

$$\hat{y} = \begin{cases} m_1^{param} & \text{if } t \in \left]-\infty, m_1^{proj}\right] \\ m_h^{param} + (t - m_h^{proj})\left(\frac{m_{h+1}^{param} - m_h^{param}}{m_{h+1}^{proj} - m_h^{proj}}\right) & \text{if } t \in \left]m_h^{proj}, m_{h+1}^{proj}\right], \ h = 1, \ldots, H \\ m_H^{param} & \text{if } t \in \left]m_H^{proj}, +\infty\right[\end{cases} \tag{4}$$

An example of the application of GRSIR to the LUT is given in Figure 1. It shows the relationship between reduced spectra and the grain size of CO_2 ice and its estimation by a piecewise linear interpolation.

4. Choice of the Look-up table

In the simulated LUT, many spectra could be superfluous to the proper estimation of the parameters. For instance, considering Tdata, spectra with parameter values not included in the Tdata's parameter range should be removed from the LUT. Better estimations can be obtained with the reduced LUT [*Bernard-Michel et al.*, 2007]. The difficulty is that, in practical cases, the range of variation of the parameters is unknown. A good strategy is to assumed a large LUT and to reduce it after the first estimation. However, the effectiveness of this technique in practical situations depends strongly on the quality of the first estimation.

In this paper, another approach is proposed that makes use of PCA to visualize the adequacy of the chosen LUT for a given set of observed spectra. The parameters of the observed spectra can be estimated only if their projections onto the first m PCA axes (deduced from the application of PCA to the LUT), coincides with the projection of the LUT itself. Conversely, to select the most appropriate spectra from the LUT for inversion, the strategy is to retain spectra from the LUT whose projections onto the PCA axes are close to projections of the spectra from the observed image (see Figure 2.(A)). In the space spanned by the first m PCA axes, the distance between each projected LUT spectrum and its nearest neighbor from the projected spectra is computed. The histogram of these distances is considered as a mixture of n_c Gaussian densities $\mathcal{N}(\mu_i, \Sigma_i)$ characterized by the proportions of the mixture $\pi_i, i \in \{1, \ldots, n_c\}$, the expectation μ_i and the covariance

matrix Σ_i of each class $i, i \in \{1, \ldots, n_c\}$. The number of classes is chosen by the user, and the parameters can be estimated by the Expectation-Maximization algorithm (EM) after random or by the K-means initialization (for further details about mixture models and EM, see *Hastie et al.* [see 2003, Sections 6.8 and 8.5]). The algorithm is a simple iterative optimization process for computing the maximum likelihood estimate of the parameters. One can then calculate and maximize the posterior probability that a spectrum belongs to a particular class by observing the aforementioned distances. This leads to a classification of the spectra into n_c classes: The class of LUT spectra that are far from the observed spectra, and those that are close. An example is given in Figure 2.(C) with the image observed from orbit 41. The histogram allows us to distinguish 3 classes. The third class corresponds well to spectra that belongs to both LUT and observed data.

Note that in Figure 2.(B) some of the observed spectra are outside the projected LUT. Since the chosen physical model is not relevant to them, these spectra are removed from the observed data. Hence, in the PCA space, the histogram of the distance of each observed spectrum with its nearest neighbor in the selected sub-LUT facilitates the distinction of two classes: The invertible spectra and the non invertible ones (Figure 2.(D)). The non invertible spectra from orbit 41 correspond to pixels at the boundary of the CO_2 bright area and thus to pixels with a linear geographical mixture of terrains. Thus, the physical model used to simulate the data is not valid. Other examples can be found in the work of *Bernard-Michel et al.* [2007]. Experimental results in the next section show that estimations are more accurate when applying such a selection.

5. Analyzing results on simulations

In this section, the competing methods are first presented. Then, the validation criteria and the parameters selection are detailed. Finally results on simulated data-sets are given.

5.1. Competing methods

***k*-NN:** From the LUT one finds the k nearest spectra and fixes the estimated y as the mean parameter value of k nearest spectra parameter. The distance between two spectra is taken as the Euclidean distance: $\|o - x_i\|^2$, where o is a spectrum from the image and x_i a spectrum from the LUT. In the experiments, k is fixed to one, so only one neighbor is used for the estimation.

Partial Least Squares regression: The PLS method is closely related to PCA (orthogonal projection onto lower dimensional space) and GRSIR (y is accounted for). PLS searches for the projection of the explanatory variable x onto a lower dimensional space that maximizes the covariance between x and y: $\max_{\beta} \operatorname{cov}^2\big(y, \beta^t x\big)$. PLS is parametrized by the size L of the subspace spanned by β. The regression in the subspace is necessarily linear and may limit the efficiency of the method if a non linear relationship exists between x and y.

Support Vector Machines regression: SVM approximates the functional F: $y = F(x)$ using a solution of the form $F(x) = \sum_{i=1}^{n} \alpha_i K(x, x_i) + b$, where x_i are samples from the training set, K a kernel function and $\Big((\alpha_i)_{i=1}^{n},\ b\Big)$ are the parameters of F which are estimated during the training process [*Scholkopf and Smola*, 2002]. The kernel K is used to produce a non-linear function. One widely used kernel is the *Gaussian Kernel*: $K(x_i, x_j) = \exp\left(-\gamma \|x_i - x_j\|^2\right)$. The SVM training entails minimization of $\left[\frac{1}{n}\sum_{i=1}^{\ell} l\big(F(x_i), y_i\big) + \lambda \|F\|^2\right]$ with respect to $\Big((\alpha_i)_{i=1}^{n},\ b\Big)$, and with $l\big(F(x), y\big) = 0$ if

$|F(x) - y| \leq \epsilon$ and $|F(x) - y| - \epsilon$ otherwise. Prior to running the algorithm, the following parameters need to be fitted: ϵ which controls the resolution of the estimation, λ which controls the smoothness of the solution and the kernel parameters (γ for the Gaussian kernel).

5.2. Validation criteria

To assess the relevance of GRSIR methodology, two aspects of the estimation were investigated: The accuracy of the estimates and the quality of the relationship between the reduced spectra and the parameters. To this end, two validation criteria were used

1. The Normalized Root Mean Square Errors (NRMSE):

$$NRMSE = \sqrt{\frac{\sum_{i=1}^{n_T}(\hat{y_i}^T - y_i^T)^2}{\sum_{i=1}^{n_T}(y_i{}^T - \overline{y}^T)^2}} \text{ with } \overline{y}^T = \frac{1}{n_T}\sum_{i=1}^{n_T} y_i^T \tag{5}$$

The NRMSE quantifies the difference between the estimations $\hat{y}_i^T$ and the real values y_i^T. This measure is normalized enabling direct comparisons between several parameter estimations. The closer NRMSE is to zero, the more accurate are the predicted values.

2. The SIR Criterion (SIRC)

$$SIRC = \frac{\beta_\ell^t(\delta)\Gamma\beta_\ell(\delta)}{\beta_\ell^t(\delta)\Sigma\beta_\ell(\delta)} \tag{6}$$

The SIRC is the ratio between the "between-slices" variance $\beta_\ell^t(\delta)\Gamma\beta_\ell(\delta)$ of the projections of $x_i, i \in \{1, \ldots, n\}$ on $\beta_\ell(\delta)$ and the total variance $\beta_\ell^t(\delta)\Sigma\beta_\ell(\delta)$ of these same projections. It quantifies the quality of the relationship between projected spectra and parameters. The closer SIRC is to 1, the better is the relationship.

5.3. Choice of the parameters

For GRSIR, the quality of the estimation $\hat{y}_i^T$ depends on a regularization parameter δ (see Section 3.1). When δ increases, the functional relationship between projected spectra and parameters gets worse and consequently estimation errors increase. On the contrary, if δ is too small, then the estimation errors are considerable in the presence of noise because the problem is ill-posed. So, the choice of δ dictates to a compromise between improving the functional relationship and increasing estimation accuracies by regularization. In this article, δ is chosen for each parameter individually, the NRMSE criterion calculated between the parameter values from a validation data and their estimations is minimized. The validation data is the look-up table itself, perturbed by multiGaussian noise representative of that affecting the OMEGA hyperspectral images (see Section 2.3). It is noted that, if there is no noise in the data, *i.e.* if the observed data exactly corresponds to spectra that could be simulated by radiative transfer model, then no regularization is required, and minimizing the NRMSE criterion for GRSIR yields a value δ close to zero.

For k-NN, since k is fixed to one, no parameter tuning is required. For PLS, the dimension L of the subspace is chosen to minimize the NRMSE on the validation set. For SVM, three parameters are fixed. ϵ is fixed to 0.01, while λ and γ are selected to minimize the NRMSE on the validation set. As it is typically done with SVM, the range of each component of Y has been stretched between 0 and 1 for the regression.

5.4. Choice of the EDR dimension

In order to choose the EDR dimension, the SIRC is calculated for each GRSIR axis $\beta_\ell(\delta)$ with $\ell \in \{1, \ldots, d\}$. As ℓ increases, the SIRC decreases rapidly and is almost zero after a few iterations. For instance, when applying GRSIR to the LUT, the SIRC for the

proportion of CO_2 ice on the first GRSIR axis is 0.985. It indicates that the relationship of interest is captured by the first axis. Calculated the second axis, the SIRC drops to 0.1799 and then is close to zero for other axes. In this case, one can consider incorporating these axes in the regression step does not bring extra information and is unnecessary, and finally fixes the EDR dimension to one. Analyzing the SIRC over all parameters and two different physical models reveals that in most situations only one dimension is necessary to retrieve the model parameters. Hence, in this article L is fitted to one.

5.5. Analyzing the GRSIR axis

The spectral variability of the x_i constituting the LUT arises from a complex interplay of the different input parameters y_i of the model. In particular, two parameters can have a similar influence on the spectra for a certain range of values. Consequently, it is crucial to understand how the GRSIR method can untangle the dependencies in order to find an independent one-to-one functional relationship between spectra and parameters. Accordingly, attempt to correlate each axis $\beta_1(\delta)$ (which is a vector of spectral weights) with the variability induced by the variation of the corresponding physical parameter. The other parameters are kept constant at mean values. The weights are individually applied to different levels of reflectance, depending on the associated wavelength, to calculate the reduced spectrum $\beta_1^t(\delta)x_i$. Hence, we find it more illustrative to represent the component wise multiplication (wavelength by wavelength) of each axis with a representative spectrum. An illustration is given in Figure 3 for the grain size of CO_2 ice. Our analysis shows that the axis for H_2O abundance, dust abundance, and grain size of CO_2 ice are quite similar. A strong weight is assigned to 1.43 micron wavelength (the bottom of a very reliable and narrow CO_2 ice absorption band) and, to a lesser extent, to the interval

between 1.47 and 1.54 microns (H_2O ice feature), and wavelengths of 1.87 and 2.29 microns (weak CO_2 ice bands but very distinct). The three axes also show differences that allow differentiation between the functional relationships. A relatively strong weight at 2.38 microns on the right wing of the 2.34 micron band is a specificity of the proportion of water ice. The axis for the proportion of dust stresses very much the variation of the spectrum continuum around 1 micron and 1.77 micron that indeed strongly changes with dust concentration. No other parameter affects the continuum as much. The axis for the grain size of CO_2 ice maximizes the influence of the small plateau at 2.62 microns that varies very much with the latter parameter. The axis that is linked to H_2O grain size is unique in the fact that it emphasizes, on the one hand, the continuum level around 1 micron, but not around 1.75 microns and, on the other hand, the entire spectral range between 2.35 and 2.65 microns. The main conclusions that can be drawn from this study are that, at least for the model presented in this paper, the GRSIR method has the ability to find a unique set of wavelengths where the variability of the spectrum is the most pertinent (but not necessary the highest) for the evaluation of a given parameter. One must note that these key wavelengths not only fall on the bottom of specific absorption bands for both H_2O and CO_2 ices but also on specific parts of the continuum as well as on specific band wings.

5.6. Results

In this section, the experimental results are compared in terms of the NRMSE and SIRC (Table 2), and also with scatter plots of real and estimated parameters (Figure 4). Except for k-NN, a spectra selection in the look-up table was performed before applying the different algorithms, as mentioned in Section 4.

From Table 2, it is clear that the worst results are obtained with k-NN. GRSIR outperforms k-NN and PLS for most parameters. Problems with the estimation of the grain size of water ice may be due to the fact that not enough values are considered for simulations in the LUT (only 5). SVM provides the best estimation in terms of the NRMSE, but with a dramatic increase in processing time: Approximately 15 hours against about 1 minute versus k-NN or GRSIR.

Figure 4 shows the scatter plot of the estimated proportions of CO_2 ice with each method versus the real proportions. It appears that the range of the estimated proportions of CO_2 ice is much larger with k-NN than with GRSIR, PLS and SVM. PLS's scatter plot is slightly curved: PLS could not handle the non linear relationship between X and Y, while GRSIR was able to model it.

It is interesting to point out that GRSIR, as a first step, can determine the ranges the parameters of an observed image are varying. Then, a more appropriate LUT can be built in the estimated ranges with a higher density of parameter values. Applying GRSIR with this new extracted LUT leads to more accurate estimations comparable to SVM, see Table 3. Finally, the SIRC, always close to 1, is very satisfying. The PLS benefits from the new LUT while the SVM does not. However, for the SVM , the processing time is decreased since the number of samples in the LUT is reduced.

6. Retrieval of the physical parameters for the south polar cap of Mars

This section summarizes the first model inversions obtained by the different algorithms for hyperspectral images acquired by OMEGA during orbits 61, 103 and 41 (see Section 2). The study of these images leads to 30 different maps. All the maps can be found in [*Bernard-Michel et al.*, 2007]. For brevity, only some are reported in the article.

The model inversion on the image observed from orbit 103 by GRSIR, PLS, SVM and k-NN shows that GRSIR and SVM give very smooth mappings for all sets of parameters. An example is given in Figure 5, where it appears that the proportion of dust is nearly always estimated at 0.0003 with k-NN, whereas with GRSIR and SVM, the map is more detailed. Some problems are encountered, with PLS: Negative values are estimated, making the map difficult to interpret.

Figure 6 shows the proportion of dust estimated by the different algorithms on the portion of the polar cap observed during orbit 41. With k-NN, estimations now assume 8 different values and seem to indicate that, at the very center of the bright cap, little dust is observed. The abundance of dust increases significantly with proximity to the boundaries. The estimated map with GRSIR is more detailed and leads to slightly different conclusions. In particular, the area presenting a poor proportion of dust is more extended than with k-NN. Nevertheless if, globally, maps are much smoother and detailed with GRSIR, they never differ entirely from k-NN's.

Another interesting remark concerns the estimation of parameters in images 61 and 103 that represent approximately the same portion of the polar cap. The analysis should consequently give close estimations for each studied parameter regardless of the method. Figure 7 shows the distribution of CO_2 grain size values obtained respectively by GRSIR, PLS on the left side (A) and SVM, k-NN on the right side (B) for both observations. Figure 8 focuses on the distribution of the estimated proportion of water and dust and on the distribution of the estimated grain size of water and CO_2 with GRSIR and SVM.

First we consider the evolution of these histograms between observations 61 and 103 for a given method. For CO_2 grain size and, to a lesser extent for H_2O grain size, a shift in

the distribution of values can be noted that is increasing when using GRSIR, then SVM, and finally k-NN. The histograms of abundances for H_2O ice and dust are relatively stable between 61 and 103 with SVM and GRSIR. The abundance for CO_2 ice would present a similar behavior since it is fully constrained (sum of abundances equals 1).

Second we note that the distributions of parameter values obtained by SVM are always shifted between to observation. The shift is always noticeable, sometimes considerable, and in addition systematically positive.

We explain these facts as follows. Observations 61 and 103 were acquired approximately 12 Mars days apart during a period of the year when the solar illumination was declining over the south pole. The conjugated effect of an increasingly grazing illumination over a slightly dusty atmosphere diminishes the spectral contrast of the observations, *i.e.* the overall level of reflectance of the spectra and on the CO_2 ice bands intensity and shape. This is very much comparable to the introduction of noise in a relative sense between observations 61 and 103. Since our remote sensing problem is partly ill-conditioned, a non regularized inversion method such as the k-NN will be much more sensitive to this noise than a regularized one such as the GRSIR or SVM. Even though regularization is thus applied to SVM, we note degraded performance when compared to GRSIR. For both methods, the estimation of the optimal value for the regularization parameter δ or λ is sensitive to the noise statistics applied to Tdata. In turn, this value determines the estimation of Y. As a consequence, uncertainties on the noise statistics propagate to bias on the estimation. We suspect that the choice of λ is less robust in the case of SVM than the choice of δ in the case of GRSIR.

Finally, for the sake of validation, the estimated maps are compared with the Wavanglet approach developed in [*Schmidt et al.*, 2007]. "Wavanglet" is a supervised automatic detection method that identifies in hyperspectral images spectral features and thus produces distribution maps of chemical compounds. It uses three steps: 1. Selection of a library composed of reference spectra (the signature of the compounds to be detected); 2. Application of a Daubechies wavelet transform to referenced spectra and determination of the wavelet subspace that best separates all referenced spectra; 3. In this selected subspace, calculation of the spectral angle between each spectrum of an observation and a given reference spectrum. In particular, this angle called the wavanglet angle, allows to quantify in a relative sense the spatial variations of the different compound abundances at the surface. The cosine of the wavanglet angle between each spectrum of the images and a reference spectrum of martian dust is presented Figure 9 . The closer it is to one, the greater the dust proportion is. A similar map is observed for the water proportion. Globally, estimates of the latter quantities are more noisy with wavanglet than with GRSIR and k-NN, especially for the dust proportion but they generally are in agreement with some exceptions. For example, in the image observed during orbit 103, k-NN, SVM, PLS and wavanglet methodologies display an area with strong proportion of dust in the lower right part of Figure 9(B), that is absent with GRSIR. In order to check if this area really contains more dust than other areas, the spectrum denoted by A in Figure 9 is selected, corresponding to the greatest proportion of dust, and compared to two other spectra from the cap. The first spectrum (B) has been chosen in a pure CO_2 area with very few dust. The second one (C) has been chosen in a area containing dust. According to k-NN, SVM, PLS and wavanglet results, this area should however contain less dust

than the area containing spectrum A. The spectra A, B and C are presented in Figure 10. One can see that, as expected, the spectrum B is really different from the spectrum A. On the other hand, spectra A and C are really similar showing that the area of interest does not contain as much dust as the wavanglet methodology predicts. On the contrary, estimations given by GRSIR are more coherent with this spectral analysis.

7. Conclusion

In this paper, a regularized version of Sliced Inverse Regression has been proposed to retrieve the physical parameters that best explain the spectra observed on Mars by the OMEGA imaging-spectrometer.

Results on simulations are promising, showing that estimations are accurate and most of the time better than the ones given by the k-nearest neighbors algorithm or PLS and close to those given by SVM. On a real data, maps are much smoother than with k-NN or PLS and seem to give a coherent mapping by comparison to the inversion of different hyperspectral images of the same portion of surface of Mars. If best results in terms of the NRMSE were obtained with SVM, the latter presents two drawbacks. First, the choice of the regularization parameter is less robust and, second, the processing time is 900 times more than GRSIR, thus making GRSIR approach more suitable for practical situations. The inversion of each new observed spectrum is really fast as well as the selection of regularization parameter. The main limitation of the proposed approach is that currently no uncertainties of the estimations are given when inverting a real image. Experimental uncertainties could be computed based on simulations, but it supposes that the noise in the spectra has been well evaluated. If not, uncertainties will probably be underestimated. Some improvements could also be proposed to choose the regularization

parameter and a more complete analysis of the influence of the noise in the GRSIR methodology would be interesting. Finally, the development of a multivariate regularized GRSIR under constraint is conceivable in order to estimate proportions simultaneously.

Acknowledgments. The authors would like to thank the reviewers for their many helpful comments. They also appreciate the contribution of Mr. Senan Doyle to this paper. This work is supported by a contract with CNES through its Groupe Système Solaire Program and by INRIA. It would not be possible also without the financial support of the "Agence Nationale de la Recherche" (French Research Agency) through its MDCO program ("Masse de Données et COnnaissances"). The Vahiné project was selected in 2007 under the reference ANR-07-MDCO-013.

References

Aster, R., B. Borchers, and T. C.H. (2005), *Parameter Estimation and Inverse Problems*, Elsevier Academic Press.

Bernard-Michel, C., S. Douté, L. Gardes, and S. Girard (2007), Estimation of Mars surface physical properties from hyperspectral images using sliced inverse regression, *Tech. rep.*, INRIA, http://hal.inria.fr/inria-00187444/.

Bernard-Michel, C., L. Gardes, and S. Girard (to appear, 2008), Gaussian regularized sliced inverse regression, *Statistics and Computing*, doi:doi:10.1007/s11222-008-9073-z.

Bibring, J.-P., et al. (2004a), *OMEGA: Observatoire pour la Minéralogie, l'Eau, les Glaces et l'Activité*, pp. 37–49, ESA SP-1240: Mars Express: the Scientific Payload.

Bibring, J.-P., et al. (2004b), Perennial water ice identified in the south polar cap of Mars, *Nature*, *428*, 627–630.

Brown, R. H., et al. (2004), The Cassini Visual And Infrared Mapping Spectrometer (Vims) Investigation, *Space Science Reviews*, *115*, 111–168, doi:10.1007/s11214-004-1453-x.

Carlson, R., M. Anderson, R. Mehlman, and R. Johnson (2005), Distribution of hydrate on Europa: Further evidence for sulfuric acid hydrate, *Icarus*, *177*(2), 461–471.

Carlson, R. W., P. R. Weissman, W. D. Smythe, J. C. Mahoney, the NIMS Science, and E. Teams (1992), Near infrared spectrometer experiment on Galileo, *Space Science Reviews*, *60*, 457–502.

Combal, B., F. Baret, M. Weiss, A. Trubuil, D. Macé, A. Pragnère, R. Myneni, Y. Knyazikhin, and L. Wang (2002), Retrieval of canopy biophysical variables from bidirectional reflectance using prior information to solve the ill-posed inverse problem, *Remote Sensing of Environment*, *84*, 1–15.

Douté, S., and B. Schmitt (1998), A multilayer bidirectional reflectance model for the analysis of planetary surface hyperspectral images at visible and near-infrared wavelengths, *Journal of Geophysical Research (Planets)*, *103*(12), 31,367–31,390.

Douté, S., B. Schmitt, R. M. C. Lopes-Gautier, R. W. Carlson, L. Soderblom, and J. Shirley (2001), Mapping SO_2 frost on Io by the modeling of NIMS hyperspectral images, *Icarus*, *149*, 107–132.

Douté, S., B. Schmitt, J.-P. Bibring, Y. Langevin, F. Altieri, G. Bellucci, B. Gondet, and the Mars Express OMEGA Team (2007a), Nature and composition of the icy terrains from Mars express OMEGA observations, *Planetary and Space Science*, *55*, 113–133.

Douté, S., E. Deforas, F. Schmidt, R. Oliva, and B. Schmitt (2007b), A Comprehensive Numerical Package for the Modeling of Mars Hyperspectral Images, in *Lunar and*

Planetary Institute Conference Abstracts, *Lunar and Planetary Institute Conference Abstracts*, vol. 38, p. #1836.

Durbha, S., R. King, and N. Younan (2007), Support vector machines regression for retrieval of leaf area index from multiangle imaging spectroradiometer, *Remote Sensing of Environment*, *107*, 348–361.

Hapke, B. (1993), *Theory of reflectance and emittance spectroscopy*, Topics in Remote Sensing, Cambridge, UK: Cambridge University Press, —c1993.

Hapke, B. (2002), Bidirectional reflectance spectroscopy: 5. the coherent backscatter opposition effect and anisotropic scattering, *Icarus*, *157*(2), 523–534.

Hastie, T., R. Tibshirani, and J. Friedman (2003), *The Elements of Statistical Learning: Data Mining, Inference, and Prediction*, Springer.

Kimes, D., Y. Knyazikhin, J. Privette, A. Abuegasim, and F. Gao (2000), Inversion methods for physically-based models, *Remote Sensing Reviews*, *18*, 381–439.

Li, K. (1991), Sliced inverse regression for dimension reduction, *Journal of the American Statistical Association*, *86*, 316–327.

Murchie, S., et al. (2007), Compact reconnaissance imaging spectrometer for Mars (CRISM) on Mars reconnaissance orbiter (MRO), *Journal of Geophysical Research (Planets)*, *112*(E11), E05S03, doi:10.1029/2006JE002682.

Philpot, W., et al. (2004), Bottom characterization from hyperspectral image data, *Oceanography*, *17*(2), 76–85.

Pragnère, A., F. Baret, M. Weiss, R. Myneni, Y. Knyazikhin, and L. Wang (1999), Comparison of three radiative transfer model inversion techniques to estimate canopy biophysical variables from remote sensing data, *Geoscience and Remote Sensing Sympo-*

sium, 1999. IGARSS '99 Proceedings. IEEE 1999 International, *2*, 1093–1095.

Schmidt, F., S. Douté, and B. Schmitt (2007), WAVANGLET: An efficient supervised classifier for hyperspectral images, *Geoscience and Remote Sensing, IEEE Transactions*, *45*(5), 1374–1385.

Scholkopf, B., and A. J. Smola (2002), *Learning with Kernels: Support Vector Machines, Regularization, Optimization, and Beyond*, MIT Press, Cambridge, MA.

Shkuratov, Y., L. Starukhina, H. Hoffmann, and G. Arnold (1999), A model of spectral albedo of particulate surfaces: implications for optical properties of the moon, *Icarus*, *137*, 235–246.

Tarantola, A. (2005), *Inverse problem theory and model parameter estimation*, Society for Industrial and Applied Mathematics.

Weiss, M., F. Baret, R. Myneni, A. Pragnère, and Y. Knyazikhin (2000), Investigation of a model inversion technique to estimate canopy biophysical variables from spectral and directional reflectance data, *Agronomie 20*, pp. 3–22.

Table 1. Sampling strategy for the simulation of the look-up table. The range of variation is given for each varying parameter as well as the number of distinct values simulated. The increment between two values is constant.

Parameters	Look-up table		Test data
	range	# distinct values	range
Proportion of water	[0.0001 0.0029]	15	[0.0006 0.002]
Proportion of CO_2	[0.9942 0.9998]	29	[0.996 0.9988]
Proportion of dust	[0.0001 0.0029]	15	[0.0006 0.002]
Grain size of water	[50 450]	5	[100 400]
Grain size of CO_2	[30000 165000]	28	[40000 105000]

Table 2. Validation criteria calculated on Tdata with GRSIR, k-NN, PLS and SVM. Note that the emphasized proportion has been fixed such that the sum of the proportions is one. For k-NN inversion the LUT contains 31500 spectra. For other methods, the LUT after selection contains 15407 spectra.

Parameters	k-NN	PLS	SVM	GRSIR	
	NRMSE	NRMSE	NRMSE	NRMSE	SIRC
Proportion of water	0.86	0.52	*0.17*	*0.40*	0.90
Proportion of CO_2	0.88	*0.56*	0.18	0.30	0.98
Proportion of dust	0.44	0.36	0.11	0.17	0.99
Grain size of water	0.43	0.44	0.17	0.54	0.84
Grain size of CO_2	0.53	0.47	0.14	0.22	0.95
CPU time	60s	181s	54,992s	58s	

Table 3. Validation criteria calculated on Tdata with GRSIR, PLS and SVM. The 3584 spectra that constitute the look-up table have been selected after a first inversion by GRSIR.

Parameters	PLS	SVM	GRSIR	
	NRMSE	NRMSE	NRMSE	SIRC
Proportion of water	0.35	*0.18*	*0.27*	0.92
Proportion of CO_2	*0.32*	0.17	0.22	0.99
Proportion of dust	0.23	0.13	0.13	0.99
Grain size of water	0.45	0.23	0.39	0.92
Grain size of CO_2	0.28	0.15	0.19	0.98
CPU time	832s	2,750s	19s	

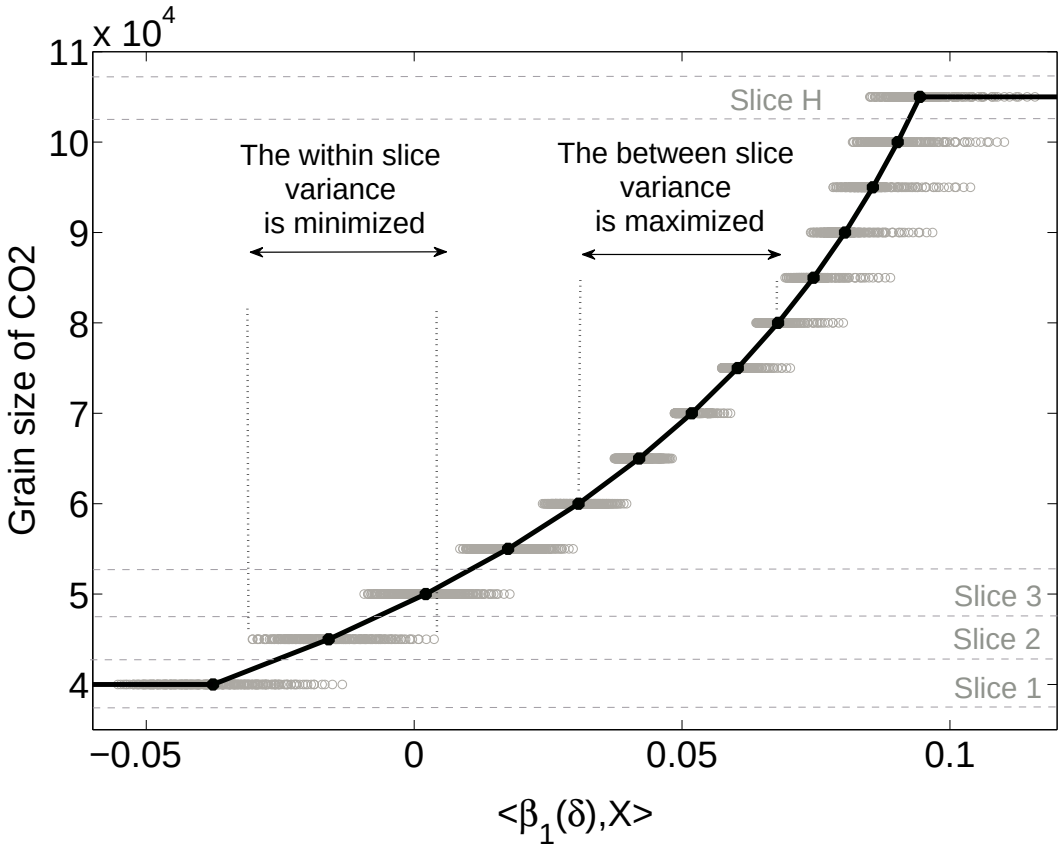

Figure 1. Functional relationship between reduced spectra on the first GRSIR axis and the grain size of CO_2 ice. This graphics illustrates the GRSIR methodology showing that the relationship is the best when the within slice variance is minimized or equivalently when the between slice variance is maximized. X-axis: reduced spectra from the learning database on the first GRSIR axis. Y-axis: Grain size of CO_2 ice.

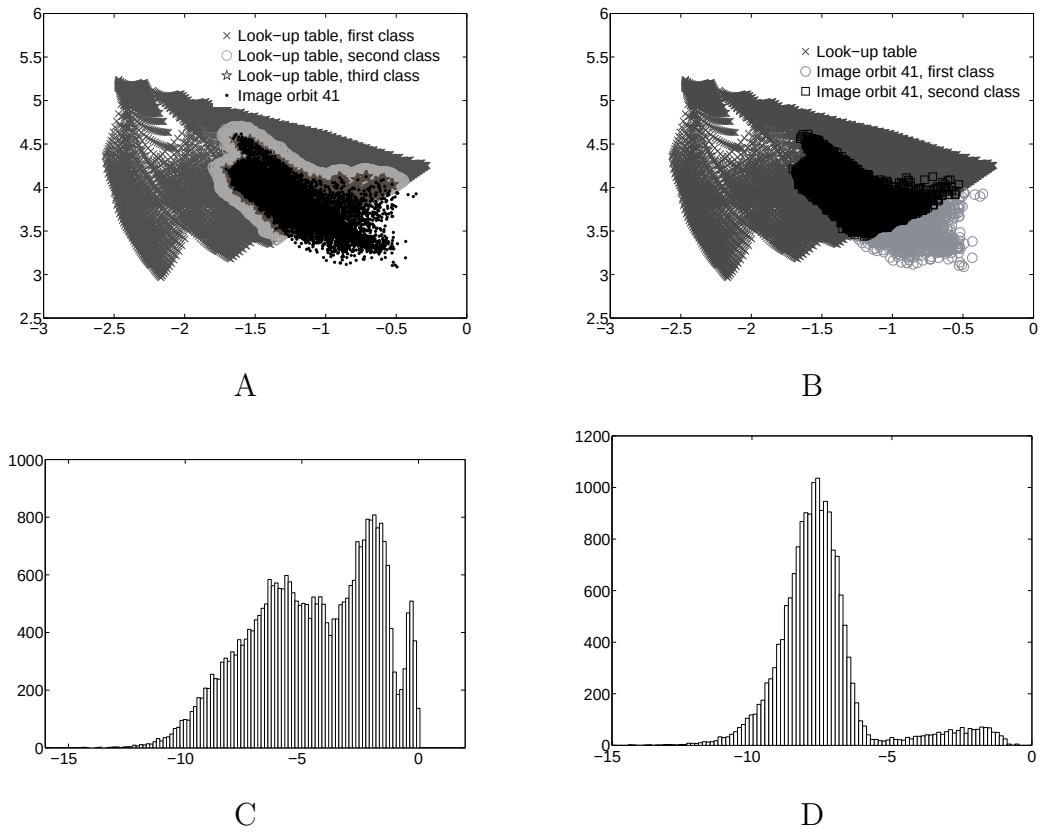

Figure 2. Selection of the *useful* spectra in the look-up table and of the *invertible* spectra in the observed data. A: Selection of a look-up table. Projections of the observed spectra from orbit 41 and the look-up table on the 2 first PCA axes (PCA applied to the look-up table). 3 classes are identified. The third class is the retained look-up table. B: Selection of invertible spectra in the image from orbit 41. The second class is retained for inversion. C: Histogram of the distances between each spectrum of the look-up table and its nearest neighbor in the image from orbit 41. D: Histogram of the distances between each spectrum of the image from orbit 41 and its nearest neighbor in the selected sub-look-up table.

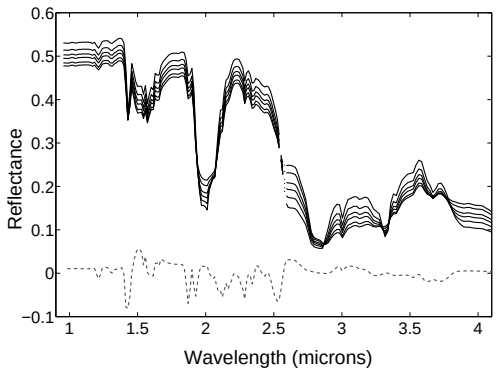

Figure 3. Plain line: Series of spectra extracted from the look-up table for CO_2 ice grain size varying between 30 and 165 millimeters, the other parameters being kept constant at mean values. Dotted-dash line: Component wise multiplication between GRSIR axis for the grain size of CO_2 ice and a representative spectrum (see Section 5.5).

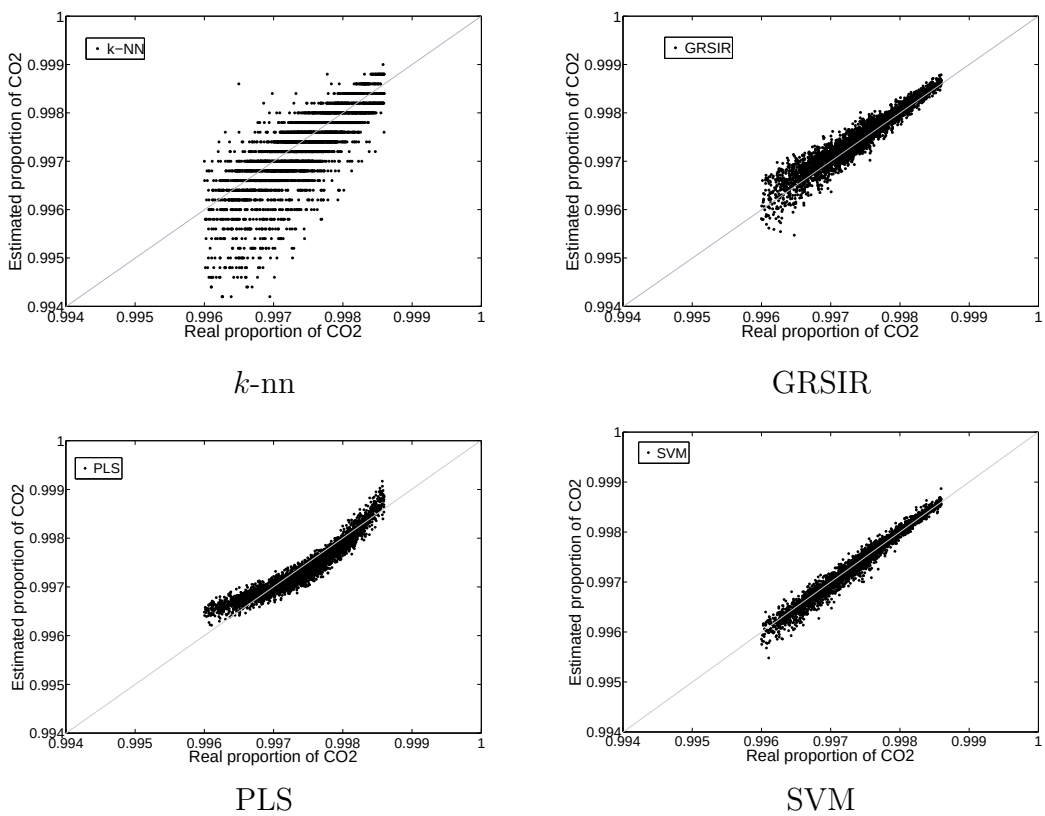

Figure 4. Scatter plots of the proportion of CO_2 ice from the test data versus estimated values. Horizontally: Proportion of CO_2 ice. Vertically: Estimated proportions of CO_2 ice by k-NN, GRSIR, PLS and SVM.

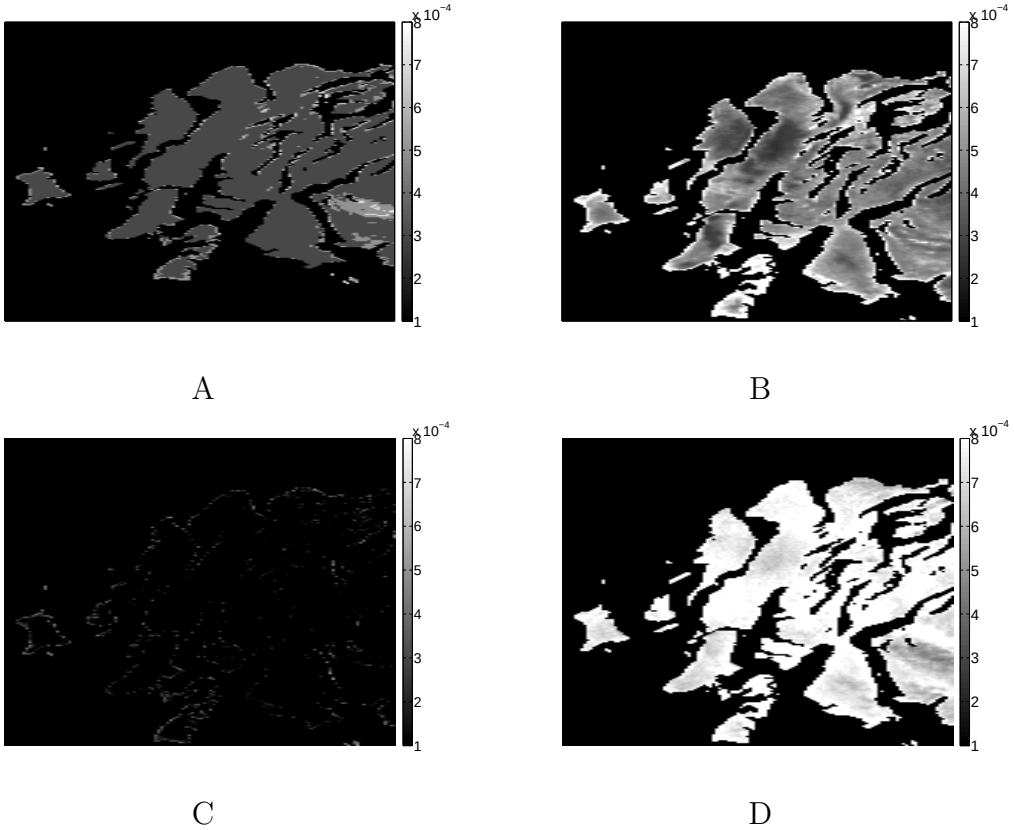

Figure 5. Proportion of dust estimated by k-NN (A), GRSIR (B), PLS (C) and SVM (D) from the hyperspectral image observed from orbit 103.

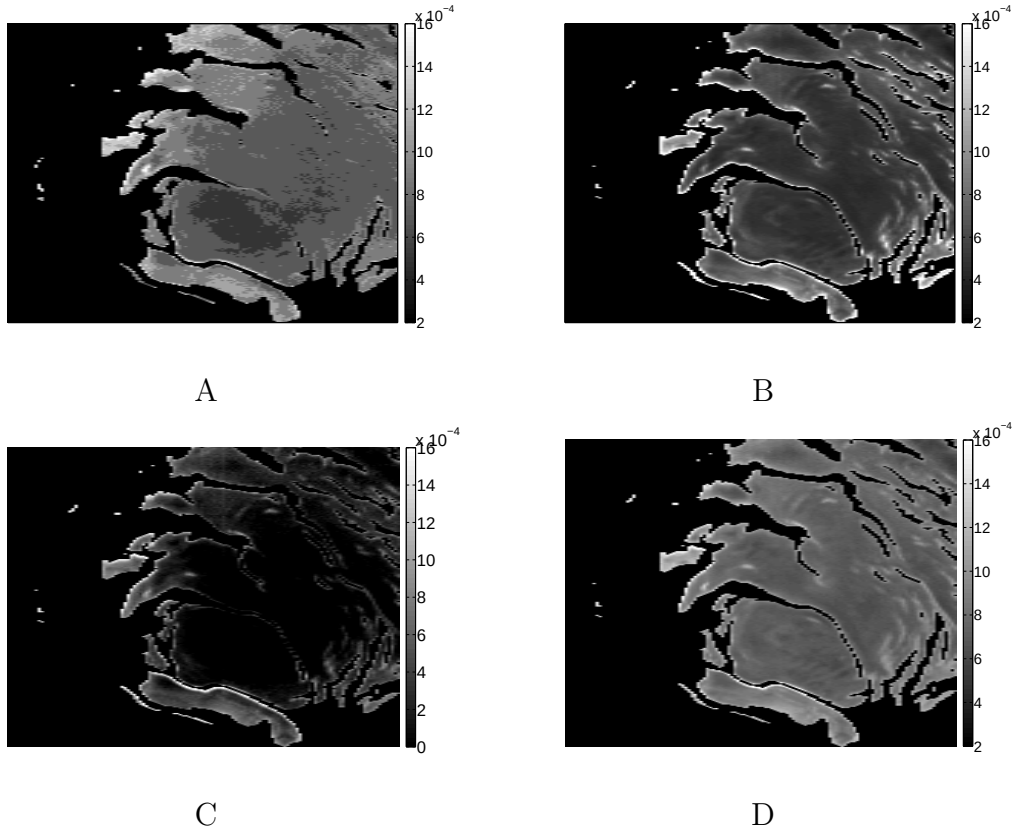

Figure 6. Proportion of dust estimated by k-NN (A), GRSIR (B), PLS (C) and SVM (D) from the hyperspectral image observed from orbit 41.

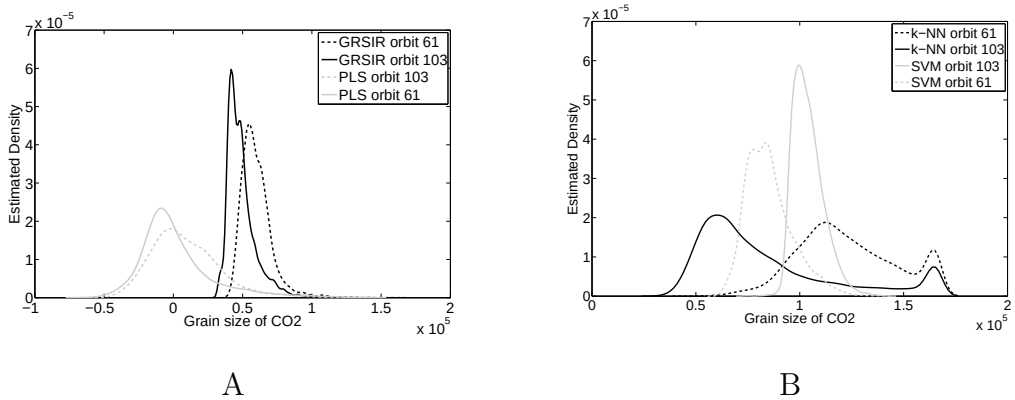

Figure 7. Comparison between the densities of the estimated grain sizes of CO_2 ice with PLS and GRSIR (A) and k-NN and SVM (B) in images from orbit 61 and 103.

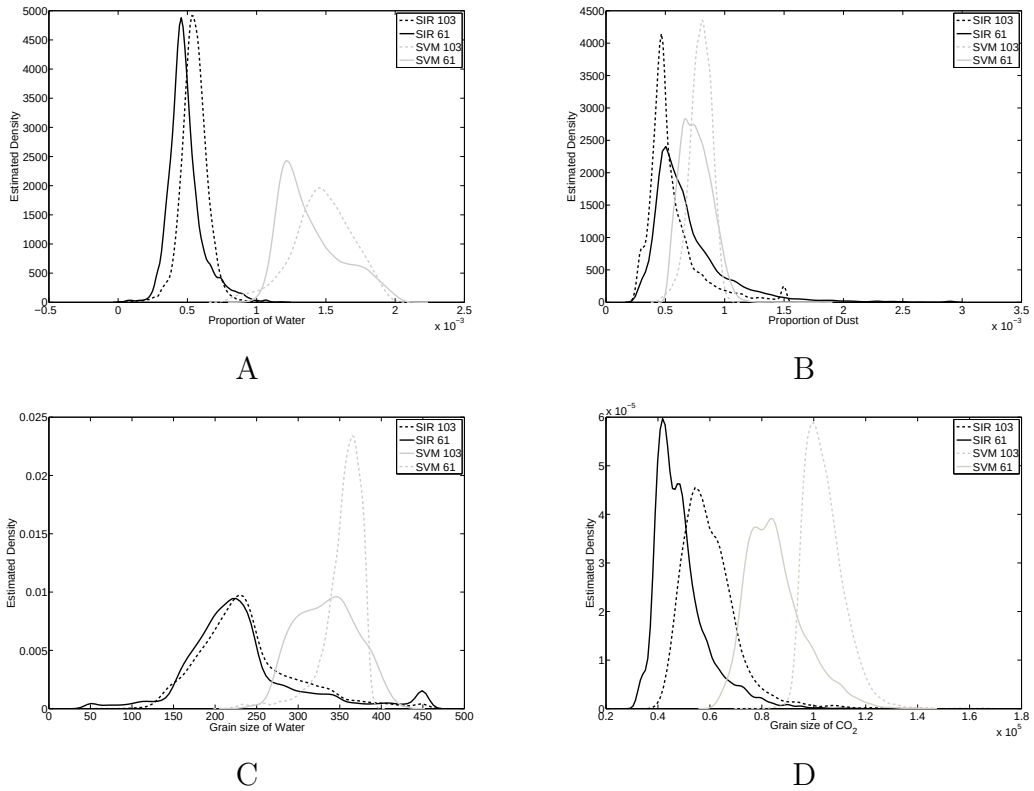

Figure 8. Distribution of values obtained for all parameters respectively by GRSIR and SVM for observations 61 and 103.

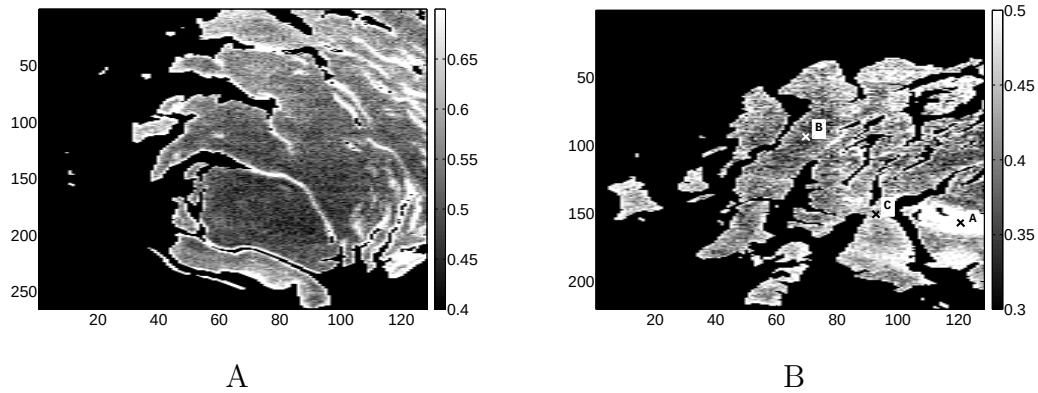

Figure 9. Cosines of the Wavanglet angle between the observed spectra and a reference spectrum of martian dust for the hyperspectral images acquired during orbit 41 (A) and during orbit 103 (B).

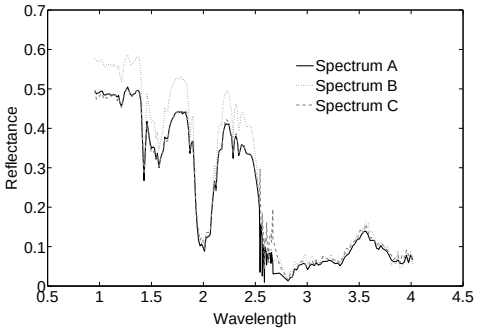

Figure 10. Spectra extracted from the locations labeled A, B and C in the image 103 of figure 9 (B).